arXiv:1601.02692v2 [cond-mat.soft] 4 Mar 2016

Embryo as an active granular fluid: stress-coordinated cellular constriction chains

Guo-Jie Jason Gao
Department of Mechanical Engineering, National Taiwan University

Michael C. Holcomb
Department of Physics, Texas Tech University

Jeffrey H. Thomas
Department of Cell Biology and Biochemistry, Texas Tech University Health Sciences Center

Jerzy Blawzdziewicz
Department of Mechanical Engineering, Texas Tech University

Mechanical stress plays an intricate role in gene expression in individual cells and sculpting of developing tissues. However, systematic methods of studying how mechanical stress and feedback help to harmonize cellular activities within a tissue have yet to be developed. Motivated by our observation of the cellular constriction chains (CCCs) during the initial phase of ventral furrow formation in the *Drosophila melanogaster* embryo, we propose an active granular fluid (AGF) model that provides valuable insights into cellular coordination in the apical constriction process. In our model, cells are treated as circular particles connected by a predefined force network, and they undergo a random constriction process in which the particle constriction probability P is a function of the stress exerted on the particle by its neighbors. We find that when P favors tensile stress, constricted particles tend to form chain-like structures. In contrast, constricted particles tend to form compact clusters when P favors compression. A remarkable similarity of constricted-particle chains and CCCs observed *in vivo* provides indirect evidence that tensile-stress feedback coordinates the apical constriction activity. Our particle-based AGF model will be useful in analyzing mechanical feedback effects in a wide variety of morphogenesis and organogenesis phenomena.

I. INTRODUCTION

Multicellular organisms utilize mechanical stress fields as a means of guiding tissue growth, triggering genetic expression and cell division, and enhancing the robustness of morphogenetic processes [1–8]. This emerging evidence of the role of mechanical feedback in orchestrating cellular-level activity has given an impetus to analyze mechanical processes involved in biological development.

While the existing evidence of the crucial role of mechanical triggering in sculpting tissues and coordinating cell behavior is indisputable, quantitative understanding of how cell communication via long-range mechanical stress fields harmonizes cell activity is fragmented and incomplete. We propose that local mechanical interactions and global stress fields in tissues can be qualitatively represented and analyzed by modeling the tissue as an active granular medium.

Tissues are a conglomeration of deformable, discrete objects (cells) that mechanically interact through direct contact and adhesion, and they are large enough for thermal motion fluctuations to be neglected. Cells, however, are not merely passive, deformable objects. They are in fact subject to genetically prescribed active deformations that can give rise to large-scale cellular flows resulting in tissue-wide structural changes. One particularly striking example of such active cellular flows is the collection of regional cellular motions (morphogenetic movements) by which an embryo changes from a single layer of cells around a yolk center into a triple-layered structure (the process known as gastrulation).

Gastrulation occurs in most animals. The active granular fluid (AGF) model proposed in this study is motivated by specific features of gastrulation in the common fruit fly (*Drosophila melanogaster*). The first morphogenetic movement of gastrulation—i.e., ventral furrow formation—is initiated by the constriction of the outer (apical) faces of the cells on what will become the underside (ventral side) of the fruit fly (see the schematic representation in Fig. 1). The constrictions produce negative spontaneous curvature of the active region of the cell monolayer, eventually leading to its invagination.

In the modeling effort presented in this study, we are concerned with the initial phase of ventral furrow formation, before the actual tissue invagination occurs. During this initial constriction phase, approximately 40% of

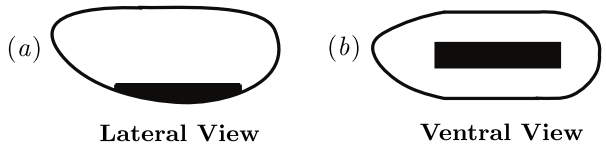

FIG. 1: Schematic of a *Drosophila* embryo with the mesoderm primordium (ventral furrow) region marked by the black stripe. (a) Lateral (side) view; (b) ventral (bottom) view. Cells in the marked region are active and in the unmarked region are passive during the initial phase of the apical constriction process.

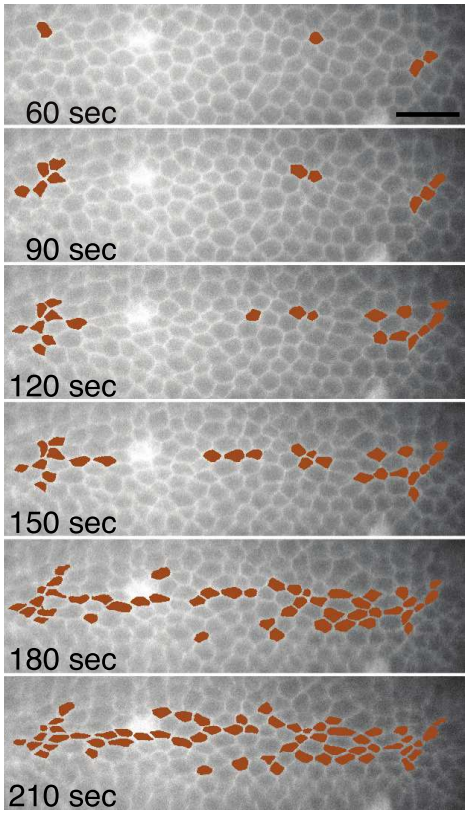

FIG. 2: Time-lapse images of the ventral side of a wild-type *Drosophila* embryo (the region indicated by the black stripe in Fig. 1) during the slow phase of the apical constriction process. Marked cells (in brown) illustrate the propagation of cellular constriction chains (CCCs). Scale bar = 20μm.

the cells gradually constrict in a seemingly random order. Furrow formation is subsequently completed with a rapid, coordinated constriction of the remaining active cells (fast phase) [9].

While apical constrictions during the initial slower phase of ventral furrow formation are generally accepted to be an uncorrelated stochastic process [9], we show here that this phase is not completely random. A close inspection of the distribution of constricted cells (see Fig. 2 and discussion in Sec. II) reveals the presence of chain-like arrangements. We call these arrangements *cellular constriction chains* (CCCs), because they are remarkably reminiscent of force chains which are observed in granular media [10, 11].

We propose that CCCs in the mesoderm primordium of the *Drosophila* embryo form as a result of coordination of cell activity through mechanical stresses. Namely, constrictions of cells (which are bonded to the surrounding cells) produce tensile stresses that propagate along tensile force chains (analogous to compressive force chains in granular matter). The presumed coupling of these strongly correlated stresses to the constriction probability of individual cells causes formation of chain-like structures of constricted cells.

We note that it was recently reported that a correlation between the rachetted contractile pulses of constricting cells had been observed [12]. However, a robust description of mechanical interactions and, possibly, coordination between the apically constricting cells has yet to be formulated.

Our approach draws on ideas developed for granular matter. Below we introduce an AGF model to describe collective cell behavior during the initial phase of apical constrictions in the ventral furrow region. We present our proof-of-concept calculations along with a qualitative comparison with *in vivo* observations.

II. EPITHELIAL TISSUE AS AN ACTIVE GRANULAR FLUID

A. A Brief review of relevant biology

Gastrulation in *Drosophila* begins around 3 hours after fertilization and is completed through multiple morphogenetic movements which are driven by region-specific cell activities [13]. These regions are established as a result of a cascading pattern formation caused by symmetry breaking events which occur during the creation of the egg (oogenesis) [14–17]. The region of cells that undergoes the apical constriction of interest is known as the mesoderm primordium and is actually internalized by ventral furrow formation.

The mesoderm primordium is composed of a band of cells on the ventral side of the embryo which take up approximately 80% of its length and 20% of its circumference [13], as schematically depicted in Fig. 1. Mesoderm primordial cells are capable of mechanical activity, due to expression of regulatory genes *twist* and *snail* [6, 18–22] established during the preceding phase of embryo patterning. Cells outside the mesoderm primordium undergo passive deformations under applied stresses, but otherwise remain mechanically inactive during the initial slower stage of ventral furrow formation [9].

B. Force chains vs. cellular-constriction chains

During the slower phase of ventral furrow formation, a growing number of mesoderm primordium cells undergo apical constriction. Initially the constrictions occur at random locations, but as time progresses the constricted cells tend to form CCCs, correlated chain-like patterns (see the highlighted cells in time-lapse images in Fig. 2; the experimental details are described in Appendix A). Similar CCC-like patterns can also be discerned in classical images available in the literature (see Fig. 4 of Ref. [9]), but to our knowledge such structures have not been explicitly reported, and their significance has not yet been analyzed.

We argue that CCCs occur as a result of coordination of apical constrictions via mechanical feedback. As discussed in Sec. I, our mechanical feedback conjecture is based on the close resemblance between CCCs and chains of interparticle forces that occur in granular media [10, 11]. In compressed or strained granular matter, individual force chains consist of a sequence of pairwise compressive forces between interacting particles that are jammed together; the chains act as a path along which the stress in the material is propagating. Similar tensile-force chains occur in systems of bonded particles [23].

Force-chain related structures have been observed in a variety of systems including emulsions, foams, and colloidal glasses [24]. Force chains, resulting from collective interactions between individual constituent particles, are a prevalent phenomenon in condensed particular matter and, therefore, we propose that they also occur in active cell packings constituting a developing tissue.

Epithelial cells in a *Drosophila* embryo are bonded to their immediate neighbors through specific protein formations (adherens junctions). Thus, both tensile and compressive stresses can be transmitted in cellular systems. The distribution of stress through force chains effectively shields the rest of the material, creating low stress regions. Assuming that the constriction probability for a given cell is affected by the forces exerted on it by the neighboring cells, such mechanical coupling may result in a non-random microstructured distribution of the constricted cells. In the following sections we examine this possibility using our AGF model.

III. ACTIVE GRANULAR FLUID MODEL

A. A simplified representation of an active cell monolayer

The cellular constrictions that motivate our AGF model occur on the outer surface of the embryonic cellular monolayer. The interior (basal) cellular ends remain relatively inactive throughout the initial slower phase of apical constrictions. Thus, to investigate coordination of the constrictions via stress distribution we can use a simplified description in which only the relevant ventral portion of the outer surface of the embryo is explicitly represented.

We approximate this area of interest (i.e., the mesoderm primordium and its immediate surroundings) as a two-dimensional plane; apical cell ends are modeled as interacting active discs that constrict in a stress-sensitive stochastic process. In the past, complex systems of strongly coupled particles (e.g., emulsions and foams) were successfully modeled using interacting disks (or spheres) [25–28]. We thus expect that using a closely packed system of active disks to approximate the mechanically excitable cell layer will reproduce the key features of the stress-driven constriction process, and will yield valuable insights into coordination of cellular constrictions by stress.

B. System geometry

Our system begins as a mechanically stable packing of N discs interacting via finite-range repulsive forces (which represent elastic cell interactions). The system, prepared using the algorithm described in Appendix B 1, occupies a square simulation box of size L. For a given particle number N and disk diameters d_i, the box size is determined from the condition that the configuration is closely packed (area packing fraction $\phi \approx 0.84$) and mechanically stable.

After the initial packing is prepared, we generate a list $\mathcal{N}_I$ of interacting neighbors. We then add attractive forces (representing cell adhesion) between the neighboring particles. Particles i and j are assumed to be the interacting neighbors, $(i,j) \in \mathcal{N}_I$, if the condition

$$r_{ij}^0 \leq 1.1 d_{ij} \tag{1}$$

is satisfied in the initial closely packed state, where r_{ij}^0 is the initial distance between the particles i and j, and $d_{ij} = \frac{1}{2}(d_i + d_j)$ is their average diameter.

In the initial state (i.e., before the disk constrictions occur), the system is a disordered 50% mixture of particles with the diameter ratio $r = 1.1$. We use the bidisperse disk system to mimic polydispersity of *Drosophila* cells and to prevent formation of hexagonal ordered structures in the initial closely packed state (such structures are not observed for cells). Subsequently, the system undergoes a sequence of particle constrictions, $d_i \to f_c d_i$, according to the algorithm described in Sec. III F. In our simulations we use the constriction factor $f_c = 0.6$, corresponding to the size of constricted cells [9].

C. Active, inactive, and constricted particles

The disks (see Fig. 3) are divided into three distinct categories: active $\mathcal{A}$ (blue particles), inactive $\mathcal{I}$ (gray), and particles already constricted $\mathcal{C}$ (brown). Inactive discs cannot undergo constriction and will remain the same size throughout the simulation. Each active disk can instantaneously constrict, and will do so by following the triggering conditions described in Sec. III F (the constricted disks cease to be active).

Particles that in the initial state are in the domain $0.25L < y < 0.75L$ are active, and the remaining particles (in the regions $0 < y < 0.25L$ and $0.75L < y < L$) are inactive. Our numerical simulations have been performed for $N = 512$ particles, so the initial stripe of the active particles is approximately 11 particles wide, similar to the width of the ventral region of active cells in a *Drosophila* embryo [9].

Our calculations are performed with periodic boundary conditions in the horizontal (anteroposterior) direction x and a free boundary in the vertical (dorsoventral)

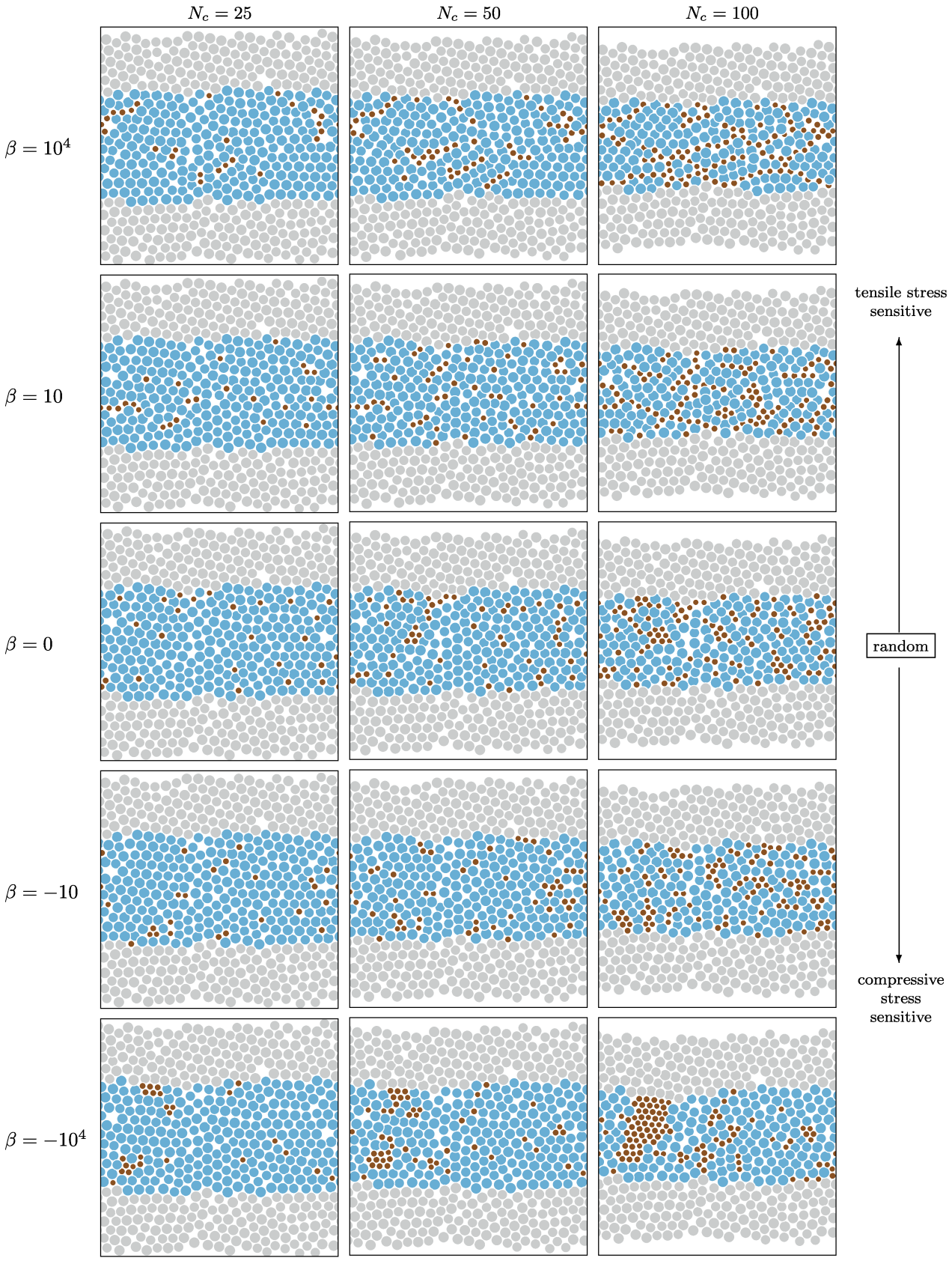

FIG. 3: Comparison of the progression of cellular constrictions for different values of sensitivity stress parameter β (as labeled) for $N_c = 25$, 50, and 100. Particle color key: active ($\mathcal{A}$) blue, inactive ($\mathcal{I}$) gray, and constricted ($\mathcal{C}$) brown.

direction y. The use of the free boundary condition is motivated by the relationship between the mesoderm primordium (the black stripe in Fig. 1) and the cells on the sides (the unmarked lateral region). Cells of the lateral regions are believed to passively deform and provide very little resistance to the apical constrictions that occur in the mesoderm primordium [9, 29]; this condition is approximated by the free boundary condition.

D. Interparticle potentials

All particles interact via the finite-range, pairwise additive, purely repulsive spring potential

$$V_r(r_{ij}) = \frac{\epsilon}{2}(1 - r_{ij}/d_{ij})^2\Theta(d_{ij}/r_{ij} - 1), \qquad (2)$$

where ϵ is the characteristic energy scale, r_{ij} is the separation between particles i and j, and $\Theta(x)$ is the Heaviside step function. In addition to the repulsion (2), the neighboring particles $i, j \in \mathcal{N}_I$ interact via the attractive spring potential

$$V_a^{\rm np}(r_{ij}) = \frac{\epsilon}{2}(1 - r_{ij}/d_{ij})^2\Theta(r_{ij}/d_{ij} - 1) \qquad (3)$$

that mimics the adhesion of neighboring cells.

In the initial state and after each particle constriction step, the system is fully equilibrated (see Appendix B 2 for details of the equilibration algorithm). Thus, the sequence of particle constriction steps is quasistatic.

E. Evaluation of particle stress

To characterize the overall stress exerted on particle i by the surrounding particles, we choose the following expression,

$$\sigma(i) = -\sum_{j\neq i}(d_{ij}/\epsilon)f_{ij}, \qquad (4)$$

where

$$f_{ij} = -{\rm d}V_{ij}/{\rm d}r_{ij}, \qquad (5)$$

with

$$V_{ij}(r_{ij}) = \begin{cases} V_r(r_{ij}) + V_a^{\rm np}(r_{ij}), & (i,j) \in \mathcal{N}_I \\ V_r(r_{ij}), & (i,j) \notin \mathcal{N}_I \end{cases} \qquad (6)$$

are the interparticle central forces (which can be tensile, $f_{ij} < 0$, or compressive, $f_{ij} > 0$). Accordingly, for $\sigma(i) > 0$ the dimensionless particle stress (4) is predominantly tensile, and for $\sigma(i) < 0$ it is predominantly compressive. The particle stress (4) is always evaluated for a system in full mechanical equilibrium, in which there is no particle motion, and all interparticle forces balance.

F. Particle constriction protocol

Particle constrictions are performed by iteratively repeating the following procedure:

a. the system is fully equilibrated;

b. particle stress $\sigma(i)$ is evaluated according to Eq. (4) for each particle i;

c. constriction probability (per one step) $P(i)$ is evaluated for each active (unconstricted) particle, $i \in \mathcal{A}$, according to Eq. (7) provided below;

d. diameters of the active particles are decreased by a factor f_c with the probability $P(i)$.

The above particle constriction step is repeated until the number of constricted particles N_c reaches a prescribed limit.

Constriction probabilities The probability $P(i, N_c)$ of constriction of particle i in a system with N_c particles already constricted is evaluated in step c of the above protocol from the expression

$$P(i, N_c) = \frac{\alpha\left\{1 + \beta\left[\sigma(i, N_c)/\sigma_{\mathcal{A}}^{\rm max}\right]^p\right\}}{(1 + |\beta|)N_a}, \qquad (7)$$

where $\sigma(i, N_c)$ is the current value of the particle stress (4), β is the stress sensitivity parameter, N_a is the current number of active particles, and

$$\sigma_{\mathcal{A}}^{\rm max} = \max_{i\in\mathcal{A}}\left[{\rm sign}(\beta)\sigma(i, N_c)\right] \qquad (8)$$

is the maximal tensile ($\beta > 0$) or maximal compressive ($\beta < 0$) stress acting on these particles. The parameter $\alpha > 0$ sets the average number of particles constricting in a single constriction step, and the parameter $p > 0$ (odd integer) determines the sensitivity profile for the dependence of the constriction process on the particle stress. We use $\alpha = 1$ and $p = 3$ in all our simulations. The chosen non-unity value of p gives a higher weight to the largest (tensile or compressive) stresses.

The parameter β determines the sign and magnitude of the overall sensitivity of particle constrictions to the particle stress $\sigma(i)$. We distinguish three fundamental cases:

1. *uncorrelated random constrictions:* $\beta = 0$;
2. *constrictions promoted by tensile stresses:* $\beta > 0$;
3. *constrictions promoted by compressive stresses:* $\beta < 0$.

In case 1, the system does not have any sensitivity to particle stresses. This purely random constriction process provides a reference system for qualitatively describing how mechanical sensitivity influences the propagation of constrictions through our medium. The other two triggering conditions introduce the sensitivity of the constriction probability to tensile stresses (case 2) or compressive stress (case 3).

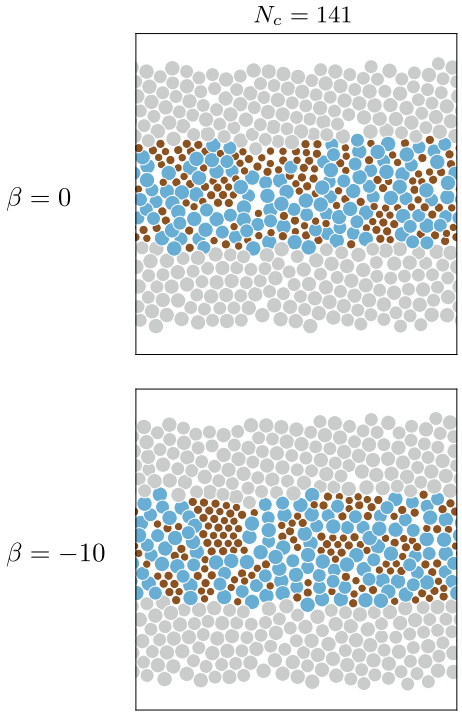

FIG. 4: Same as Fig. 3, but for a larger value of N_c.

The simulations for the stress-dependent cases were performed at a variety of β values. Representative results, for $\beta = \pm 10$ (moderate stress sensitivity) and $\beta = \pm 10^4$ (strong stress sensitivity), are discussed below.

IV. RESULTS AND DISCUSSION

Here we describe the results of our numerical simulations of correlated particle constrictions in the AGF model introduced in Sec. III. We discuss the evolving microstructure of constricted-particle regions and analyze the stress distribution for different signs and magnitudes of the stress sensitivity parameter β in the constriction probability function (7), to determine mechanisms that control the constriction patterns.

We focus on the initial stage of the system evolution, until approximately 40% of particles have constricted, because this stage is most relevant to the initial phase of ventral furrow formation in the *Drosophila* embryo. However, since our results may be relevant also to other systems of mechanically active cells, we examine a variety of constriction triggering conditions and provide a limited set of results for longer times.

All simulations are performed for the same initial condition with $N_a^0 = 258$ initially active particles. Thus, for $N_c = 25$ approximately 10% particles have constricted, for $N_c = 50$ approximately 20%, and for $N_c = 100$ approximately 40%.

A. Microstructural evolution

The results of our numerical simulations of the microstructural evolution are summarized in Figs. 3 and 4 [also see Movies 1(a)–1(e) in Supplementary Data]. The presented images of particle configurations reveal that the spatial arrangement of the constricted particles shows a striking dependence on the sign and magnitude of the constriction-triggering stress.

In systems in which particle constrictions are induced by *tensile stress* (the top two rows of images in Fig. 3), constricted particles form strongly correlated *chain-like structures*, which closely resemble CCCs that we have identified in the *Drosophila* embryo (see Fig. 2). In contrast, the microstructure of the system in which active particles are sensitive to *compressive stresses* (the bottom two rows of images in Fig. 3) is dominated by compact constricted-particle *clusters*.

The chains that form for $\beta > 0$ are partially aligned with the x-direction (i.e., the direction of the system periodicity). The chains are initially disconnected (see the images for $N_c = 25$ and 50), but at later times ($N_c = 100$ for $\beta = 10^4$) they grow into a percolating network spanning the system in the x-direction. This behavior closely resembles the constricted-cell dynamics in the mesoderm primordium shown in Fig. 2. Our results thus provide powerful (though indirect) evidence of the tensile-stress feedback involved in cellular constrictions in the early phase of ventral furrow formation in the *Drosophila* embryo.

The chaining is most pronounced for large magnitudes of the stress sensitivity parameter β. We find that for a moderate value $\beta = 10$, the chains are fragmented and less aligned with the x-axis than for $\beta = 10^4$; and percolation occurs later, at $N_c \approx 130$ [see Movie 1(b) in Supplementary Data].

In systems with particle constrictions induced by compressive stresses, $\beta < 0$, we observe the formation of compact clusters, with significant size polydispersity and inhomogeneous spatial distribution. The clusters remain disconnected and do not percolate, until much later in the process.

For a moderate sensitivity-parameter value $\beta = -10$, the clusters are much smaller than for the system with strong stress sensitivity $\beta = -10^4$. In fact, during the evolution stage depicted in Fig. 3, the cluster distribution in systems with $\beta = -10$ and $\beta = 0$ (no stress sensitivity) looks similar; however, at later stages the difference between the fully random and weak-stress-sensitivity systems becomes much larger (see Fig. 4).

We note that even in a fully random case, $\beta = 0$, a significant number of clusters form already at a relatively early stage of evolution (see Fig. 3 for $N_c = 50$). This is because an isolated constricted particle typically has several active neighbors, which increases the probability of formation of small groups of constricted particles in an uncorrelated random process.

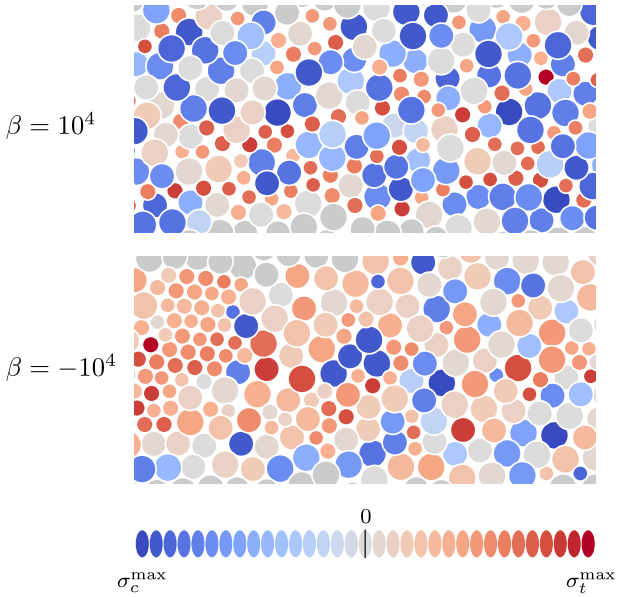

FIG. 5: A visual representation of the distribution of stress σ through the active region of a granular fluid at $N_c = 100$ and β as labeled. Shades of blue and red show a net compressive and tensile stress, respectively. (The color scale is relative to the maximal compressive and tensile stresses in the system $\sigma_c^{\max}$ and $\sigma_t^{\max}$.)

B. The mechanism of chain and cluster formation

To elucidate the mechanisms of chain and cluster formation, we examine the stress distribution in the evolving AGF undergoing particle constrictions. A color map of the particle stress, Eq. (4), is presented in Fig. 5 for a system with constrictions triggered by tensile stresses (top panel, $\beta = 10^4$) and compressive stresses (bottom panel, $\beta = -10^4$). Both panels show the same stage of the evolution, $N_c = 100$. The images were obtained by recoloring the corresponding panels in Fig. 3, to visualize the distribution of stress in the active particle band. Movies 2(a) and 2(b) in Supplementary Data show the evolution of the stress distribution during the constriction process.

A close examination of the top panel of Fig. 5 reveals the following key features of the stress distribution that are essential for understanding the microstructural evolution (see the schematics in Fig. 6):

1. chains of constricted particles are predominantly subject to tensile stress;

2. unconstricted particles that are positioned alongside the chain are predominantly compressed, while those near the chain ends are predominantly under tension.

In a system sensitive to tensile stresses (Fig. 6(a)), active particles are most likely to constrict near the ends of an already formed chain, because the tensile stress is predominant in these regions (as indicated by the dashed red circles in Fig. 6(a) and the tensile stress coloring in Fig. 6(c)). Thus the chain increases in length. This mechanism not only promotes chain growth, but also results in increased chain connectivity, stimulating the expansion of a constricted-particle-chain network, and leading to its eventual percolation.

In a system sensitive to compressive stresses (see Fig. 6(b)), the above mechanism of growth of a constricted region is inverted: the compressed particles alongside the chain (i.e., in the regions indicated by the dashed blue ovals) are now likely to constrict, which results in restructuring of the chain into a compact cluster. A similar mechanism governs growth of already formed clusters.

C. Evolution of the particle stress distribution

A comparison of the stress distribution for a tensile-stress-sensitive system (top panel of Fig. 5) and for a compressive-stress-sensitive system (bottom panel of Fig. 5) shows that the stresses are distributed very differently. For tension-sensitive triggering, the tensile stress propagates along a network of constricted-particle chains, leaving pockets of compressive stress between the chains. In contrast, for compression-sensitive triggering (i.e., when a network of constricted particles does not form), the tensile stress distribution is much more uniform, and, moreover, the tensile stresses are predominant, and only small pockets of compressive stress remain.

To gain further insights into stress feedback mechanisms that may be important in ventral furrow formation (and more generally in behavior of active particulate systems), we examine the evolution of particle stress for different particle populations. The distribution of particle stress for the populations of active particles $\mathcal{A}$, constricted particles $\mathcal{C}$, and inactive particles $\mathcal{I}$ is shown in Fig. 7 for a tensile-sensitive system with $\beta = 10^4$. Figure 8 shows the corresponding results for the particle pressure

$$\bar{\sigma} = -\sigma \tag{9}$$

in a compression-sensitive system with $\beta = -10^4$. (We call quantity (9) the particle pressure, in line with the standard convention in fluid mechanics, in which the pressure tensor is the negative of the stress tensor.)

In both cases the results are sorted from the smallest to largest value of the stress σ (pressure $\bar{\sigma}$) and shown vs. particle index i_p. Accordingly, the largest triggering stress (pressure) corresponds to the upper-right end of the curves representing the stress (pressure) distribution.

The results reveal several important features common to all particle populations and both constriction-triggering conditions. First, the slope of the curves sharply increases near the ends of the curves $\sigma(i_p)$ and $\bar{\sigma}(i_p)$. This behavior indicates that there exist small particle subsets for which the stress σ (or pressure $\bar{\sigma}$) significantly differs from the stress (pressure) for typical particles. Second, the stress distribution is initially

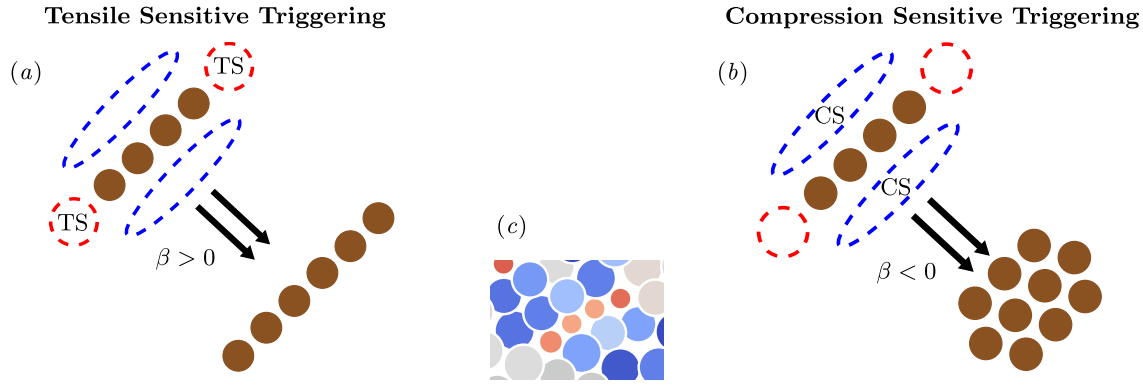

FIG. 6: Mechanism of formation of (a) chains and (b) clusters of constricted particles (brown circles); and (c) the distribution of particle stress (color scale as in Fig. 5) near a chain of four constricted particles. Areas of tensile stress (TS, red dashed circles) and areas of compressive stress (CS, blue dashed ovals) denote regions of tensile-stress- and compressive-stress-triggered constrictions, respectively.

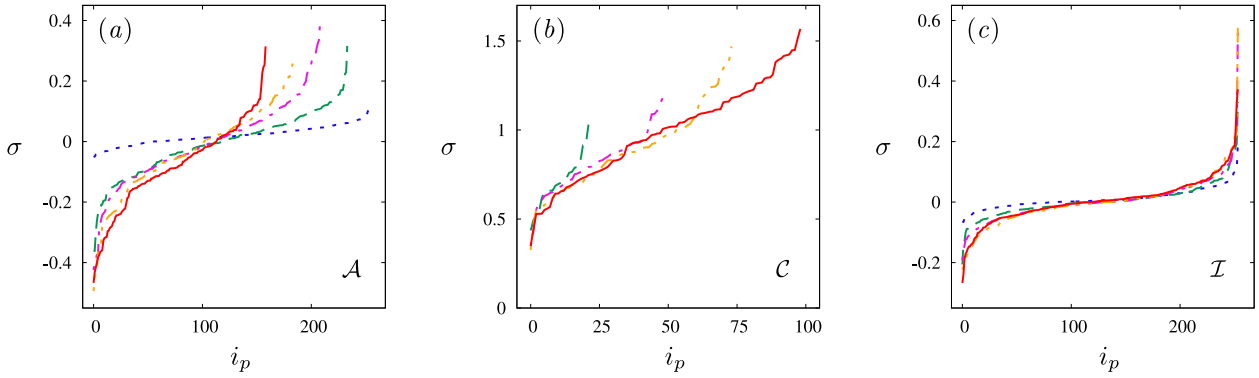

FIG. 7: Stress distribution $\sigma = \sigma(i, N_c)$ for (a) active, (b) constricted, and (c) inactive particles, in a system sensitive to tensile stress ($\beta = 10^4$), with $N_c = 0$ (blue dotted line), $N_c = 25$ (green dashed), $N_c = 50$ (purple dash–dot), $N_c = 75$ (orange dash–dot–dot), and $N_c = 100$ (red solid) constricted particles. For a given N_c, the results are sorted by the increasing value of stress and shown vs. particle index i_p.

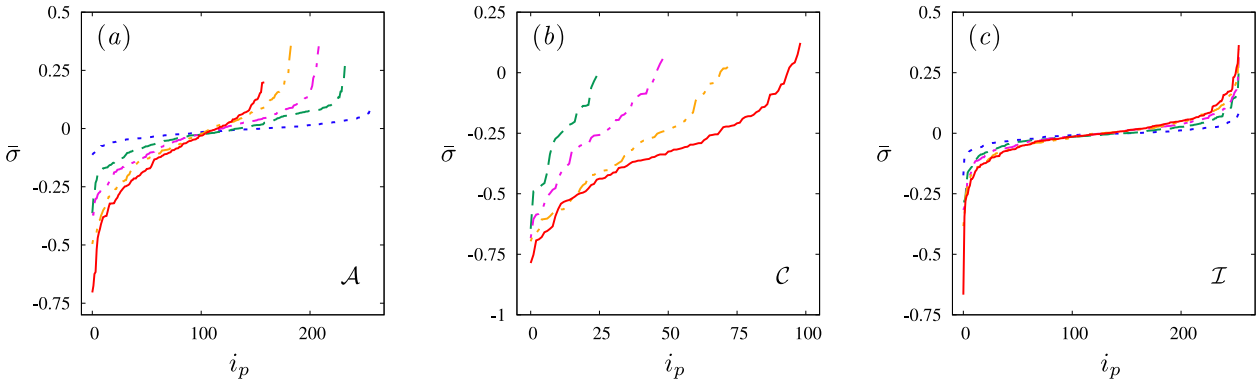

FIG. 8: Same as Fig. 7, but for a system sensitive to compressive stress ($\beta = -10^4$), and for the values of the particle pressure $\bar{\sigma} = -\sigma$.

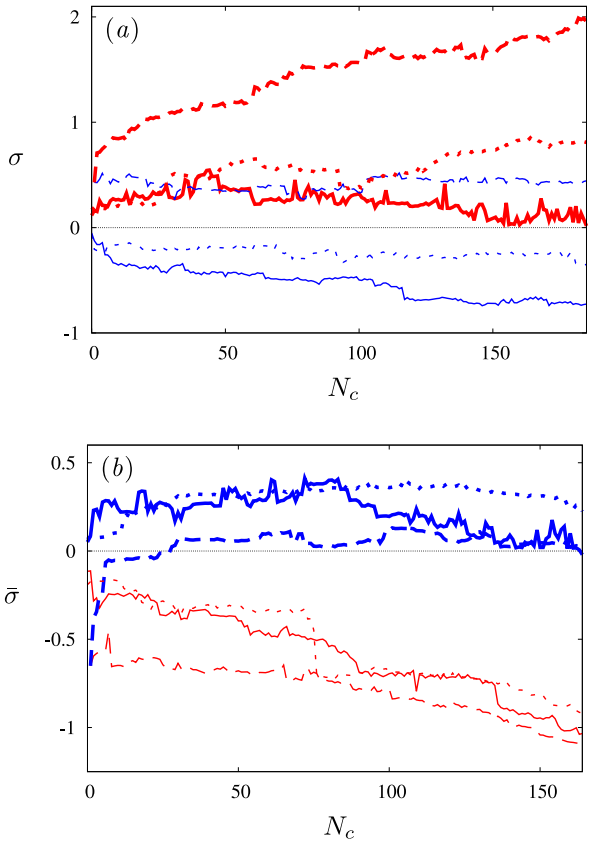

FIG. 9: (a) Evolution of the maximal stress $\sigma = \sigma^{\max}$ (thick lines) and minimal stress $\sigma = \sigma^{\min}$ (thin lines) in a system with stress sensitivity parameter $\beta = 10^4$ for the three types of particles: active (solid lines), constricted (dashed), and inactive (dotted). (b) The same as (a), except that for a system with $\beta = -10^4$ and for the values of particle pressure $\bar{\sigma} = -\sigma$. In both panels, the red lines correspond to the tensile end of the stress range, and blue ones to the compressive end.

narrow, and becomes significantly wider when particles start to constrict creating local inhomogeneities within the medium, and generating large positive and negative values of particle stress. The latter feature of the stress distribution is also visible in Fig. 9, where the minimal and maximal particle stress

$$\sigma^{\min}(N_c) = \min_{i\in\mathcal{P}} \sigma(i, N_c), \qquad \sigma^{\max}(N_c) = \max_{i\in\mathcal{P}} \sigma(i, N_c), \tag{10a}$$

and particle pressure

$$\bar{\sigma}^{\min} = -\sigma^{\max}, \qquad \bar{\sigma}^{\max} = -\sigma^{\min} \tag{10b}$$

in the population $\mathcal{P} = \mathcal{A}, \mathcal{C}, \mathcal{I}$ are plotted versus the number of constricted particles for tension- and compression-sensitive systems.

Tensile-stress-sensitive triggering The results depicted in Figs. 7(a) and 9(a) show that the maximal tensile stress in the population of active particles $\mathcal{A}$ in a tension-sensitive medium initially increases, but subsequently gradually decreases, and eventually vanishes. The non-monotonic behavior of the tensile stress in the population $\mathcal{A}$ is a consequence of the formation of a network of connected constricted-particle chains which support most of the tensile stress (see Fig. 3 and the top panel of Fig. 5).

Because the constriction probability (7) is normalized by the maximal stress (8) in the current configuration, our simulations cannot be continued beyond the point at which the maximal tensile stress in the active population $\mathcal{A}$ vanishes. In a modified model with normalization by a fixed characteristic stress, the constriction process could be continued, but would significantly slow down at the point $\sigma_{\mathcal{A}}^{\max} \approx 0$. (In wild type *Drosophila* the slowdown would not occur because of the earlier transition to the rapid phase of apical constrictions, which is controlled by different mechanisms; the slowdown, however, could perhaps be observed in *Drosophila* mutants.)

The growth of the stress-supporting network of constricted particles is reflected in a steadily increasing stress in the particle population $\mathcal{C}$ (see Fig. 7(b) and the dashed red line in 9(a)). We hypothesize that the stress-supporting network of CCCs in the *Drosophila* embryo (analogous to the interconnected constricted-particle chains in our AGF model) plays a biologically useful role. First, since the chains distribute stresses non-locally in the entire active region, they may mitigate the effect of decreased cell contractility in some domains (such domains may result from random fluctuations or genetic defects). Second, a tightly stretched band of interconnected CCCs may help to organize a coherent tissue motion at the onset of the second phase of ventral furrow formation. In both cases, CCCs would contribute to robustness of the invagination process. However, the role of CCCs requires further investigations.

Compressive-stress-sensitive triggering As discussed at the beginning of Sec. IV C, compression-sensitive systems develop large continuous areas of tensile stress. These areas include compact domains of active and constricted particles. As a consequence of this morphology, the tensile stress (i.e., the negative pressure $\bar{\sigma}$ in the plots shown in Figs. 8 and 9(b)) is similarly distributed in the populations $\mathcal{A}$ and $\mathcal{C}$. As seen in Fig. 9(b), the tensile stress is somewhat larger for constricted particles (red dashed line) than for active particles (red solid line), but the difference is much smaller than the corresponding difference for tension-sensitive triggering (see dashed and solid red lines in Fig. 9(a)).

The compressive stress (i.e., the positive pressure $\bar{\sigma}$) is less evenly distributed. In the population of active particles $\mathcal{A}$, the maximal value $\bar{\sigma}^{\max}$ is relatively small and decreases to zero at long times. Only a few constricted particles are under compression according to the stress map shown in the bottom panel of Fig. 5, and the maximal pressure is negative or close to zero during the entire evolution.

We note that the behavior of the stress distribution within the population of constricted particles $\mathcal{C}$ is qualitatively different in the compression-sensitive medium

(see Fig. 8(b)) and the tension-sensitive medium (see Fig. 7(b)). In the former case, the slope of the curve $\bar{\sigma} = \bar{\sigma}(i_p)$ decreases with the increasing N_c, and in the latter case the slope of the corresponding curve $\sigma = \sigma(i_p)$ remains constant (only the middle, nearly linear, part of the curve varies in length). This universal slope is likely to be a signature of scaling properties of the developing constricted-particle network.

Behavior of the inactive region As depicted in Figs. 7(c) and 8(c), the stress distribution in the inactive-particle region $\mathcal{I}$ is relatively featureless. Most of the particles experience small positive or negative stresses, and, according to stress maps (not shown) only a small number of particles on the border between the active and inactive regions are affected by particle constrictions. The maximal tensile stress grows with N_c, and the compressive stress saturates (see Fig. 9).

With the free boundary condition in the y-direction, the inactive particles do not affect the active region in a significant way. However, for more resistive boundary conditions (e.g., periodic boundary conditions in both x and y directions; results not shown), the interaction between the passive and active regions is much stronger. In our future studies, this effect will be investigated in the context of interactions between active cells in the mesoderm primordium and the surrounding cells in more lateral regions.

V. CONCLUSIONS

Mechanical stress fields are now believed to play a pivotal role in many biological developmental processes. Therefore, it is crucial to establish methods to investigate local cell–cell mechanical interactions and global stress distributions across tissues and evaluate the effect of such local and global phenomena on mechanical cell activity. We have shown that modeling a tissue as an active granular medium can offer a means of analyzing mechanical feedback involved in tissue development.

Our AGF model of apical constrictions in the *Drosophila* embryo during the early stage of ventral furrow formation has demonstrated constriction patterns that are qualitatively similar to those observed *in vivo*. The key new element of the model is the quantification of the mechanical sensitivity of cells to tensile stresses, which are responsible for an increase in the cell constriction probability. The agreement between the model predictions and constriction patterns observed in the *Drosophila* mesoderm primordium provides evidence of the role of mechanical feedback in the early stage of morphogenesis examined here.

We have considered a wide range of constriction triggering conditions and analyzed the associated stress distribution, which evolves as the cellular constriction process progresses. We have also shown that in systems in which cells are sensitive to compressive stresses, growing clusters of constricted particles are formed instead of constricted-particle chains. It follows that mechanical feedback can be used to control the system morphology.

The cell dynamics during the initial apical constriction phase of ventral furrow formation (considered here) can be modeled using a 2D AGF approach, because cells at this stage are mechanically active only in a narrow, nearly planar region. However, subsequent morphogenetic movements (e.g., the later phase of ventral furrow formation, cephalic furrow formation, and germ band extension) involve large-scale collective cell motions in different mechanically coupled domains. Understanding the role of mechanical feedback in coordinating cell activity will thus require development of comprehensive full-embryo 3D models in which motion of all cells (approximately 6000), arranged in an epithelial monolayer surrounding the yolk sac, will be explicitly followed; we are working on such models.

We expect that a variety of morphogenetic and organogenetic processes can be studied by modeling a developing tissue as an active granular fluid. For example, mechanical stresses have been shown to influence multiple aspects of heart development in Zebrafish. Stress exerted upon cells by fluid flow influences the number of chambers which are developed [30], valve growth [31], and the establishment of pacemaker cells. It is possible that these mechanically sensitive aspects of cardiogenesis can be evaluated by considering an appropriate AGF model.

Statistical mechanics methods and simulation techniques that were initially developed for investigations of complex fluids have significantly contributed to the understanding of molecular-level mechanisms in biological systems. In particular, fundamental studies of protein folding [32–34] (also advanced by George Stell's group [35–37]) have led to the development of designer proteins [38–40]. Other examples of cross-pollination between fluid-state physics and biology include rapid progress in areas such as cytoskeleton dynamics [41–43] and behavior of cell membranes [44–46].

We anticipate that studies of the collective phenomena associated with mechanical cellular activity and intercellular interactions, including results of multicellular modeling of mechanical feedback during tissue formation, will be of similar importance for understanding morphogenesis and organogenesis. Further, the knowledge gained will also lead to applications in tissue engineering.

ACKNOWLEDGMENTS

GJG gratefully acknowledges financial support from NTU startup funding 104R7417. Imaging experiments were supported by funds from TTUHSC to JHT.

Appendix A: Imaging a *Drosophila* embryo

The ventral surfaces of live *Drosophila melanogaster* embryos were imaged to observe the constriction of cell apices during ventral furrow formation [22]. Cell apices were visualized by the fluorescently labeled plasma membrane protein encoded by the *Spider-GFP* transgene [47]. Embryos were prepared for imaging, selected by age under the dissecting microscope, oriented and glued to coverslips as described [22, 48, 49]. To avoid any artifacts caused by gluing the vitelline membrane of the ventral surface of the embryo to the coverslip that we imaged through, we designed and constructed an imaging chamber. The bottom of the chamber consisted of a coverslip with a strip of embryo glue flanked on either side by two layers of double-sided Scotch tape. Two layers of double-sided Scotch tape are sufficient to avoid compression of the embryo [50]. The dorsal sides of the embryos were glued to the bottom of the imaging chamber and the embryos were covered with halocarbon oil 27 (Sigma). A number 1.5 coverslip was adhered to the double-sided tape to close the chamber and allow the ventral surfaces of the embryos to be visualized. The imaging chamber was taped to a glass slide. Images were collected every 10 seconds using a Zeiss Axio Imager.A1 microscope with Axiovision 4.4 software. Time-lapse images were compiled using Axiovision and ImageJ [51]. Images were processed and constricted apices marked using Photoshop. Constricted apices were indicated based on the widths in the smallest dimension of the cell apex and its evolution over time.

Appendix B: Numerical simulation details

1. Preparation of the initial disk configuration

To prepare the initial disk configuration for our numerical simulations of the correlated apical constriction process, we (a) generate a random close packing (RCP) of frictionless disks interacting via the finite-range repulsive potential (2); (b) establish the neighbor list $\mathcal{N}_I$ according to the criterion (1); (c) add the attractive potential (3); and (d) equilibrate the system.

The required RCP of disks is prepared by following the packing-generation procedure described in [52]. Accordingly, the disks are randomly placed in a square unit cell with periodic boundary conditions. The particle diameters are then increased or decreased by a gradually decreasing factor, to remove overlaps or gaps between particles; the particle size change is followed by energy minimization. The process is repeated until there is no room to change the size of particles without creating an overlap [52].

2. System equilibration

Nonequilibrium configurations arising during the initial-state generation and after each particle contraction are equilibrated using molecular dynamics of a dissipative system with the interparticle central potential forces

$$\mathbf{f}_{ij} = f_{ij}\hat{\mathbf{r}}_{ij}, \tag{B1}$$

and velocity-dependent dissipative resistance forces $\mathbf{f}_{ij}^{\rm diss}$. Accordingly, the equations of motion

$$m_i\mathbf{a}_i = \sum_{j\neq i}(\mathbf{f}_{ij} + \mathbf{f}_{ij}^{\rm diss}) \tag{B2}$$

(where m_i and $\mathbf{a}_i$ are the mass and acceleration of particle i, and $\hat{\mathbf{r}}_{ij}$ is the unit vector pointing from the center of particle j to i) are solved using the velocity Verlet algorithm, until the system reaches the energy minimum.

During the initial packing preparation we use

$$f_{ij} = -{\rm d}V_r(r_{ij})/{\rm d}r_{ij} \tag{B3}$$

and

$$\mathbf{f}_{ij}^{\rm diss} = -b\Theta(d_{ij}/r_{ij} - 1)(\mathbf{v}_{ij}\cdot\hat{\mathbf{r}}_{ij})\hat{\mathbf{r}}_{ij}, \tag{B4}$$

where $\mathbf{v}_{ij} = \mathbf{v}_i - \mathbf{v}_j$ is the relative velocity between particles i and j, and b is the resistance constant. During the subsequent process of particle constrictions we use the potential force (5) and

$$\mathbf{f}_{ij}^{\rm diss} = \begin{cases} -b(\mathbf{v}_{ij}\cdot\hat{\mathbf{r}}_{ij})\hat{\mathbf{r}}_{ij}, & (i,j)\in\mathcal{N}_I \\ -b\Theta(d_{ij}/r_{ij}-1)(\mathbf{v}_{ij}\cdot\hat{\mathbf{r}}_{ij})\hat{\mathbf{r}}_{ij} & (i,j)\notin\mathcal{N}_I \end{cases} \tag{B5}$$

(i.e., attractive and dissipative interactions between nonoverlapping neighbors are also included).

The equilibration is performed with $b = 0.5$ in the dimensionless units where the diameter d_s and mass m_s of the small particles and the interparticle potential amplitude ϵ are chosen as the reference length, mass, and energy scales. The mass of the large particles is $m_l = m_s r^2$, where r is the initial diameter ratio; the particle masses m_s and m_l are not affected by constrictions. We note that the particle masses and the specific form of the dissipative resistance forces influence only the numerical efficiency of the equilibration process, but do not affect the final equilibrated state.

[1] T. Mammoto and D.E. Ingber. Mechanical control of tissue and organ development. *Development*, 137(9):1407–1420, 2010.

[2] C.J. Miller and L.A. Davidson. The interplay between cell signalling and mechanics in developmental processes. *Nat. Rev. Genet.*, 14(10):733–744, 2013.

[3] H. Zhang and M. Labouesse. Signalling through mechanical inputs - a coordinated process. *J. Cell Sci.*, 125(13):3039–3049, 2012.

[4] Y.-T. Shiu, J.A. Weiss, J.B. Hoying, M.N. Iwamoto, I.S. Joung, and C.T. Quam. The role of mechanical stresses in angiogenesis. *Crit. Rev. Biomed. Eng.*, 33(5):431–510, 2005.

[5] E. Farge. Mechanical induction of twist in the Drosophila foregut/stomodeal primordium. *Curr. Biol.*, 13(16):1365–1377, 2003.

[6] P.-A. Pouille, P. Ahmadi, A.-C. Brunet, and E. Farge. Mechanical Signals Trigger Myosin II Redistribution and Mesoderm Invagination in Drosophila Embryos. *Sci. Signal.*, 2(66), 2009.

[7] T. Idema and A.J. Liu. Mechanical signaling via nonlinear wavefront propagation in a mechanically-excitable medium. *Phys. Rev. E*, 89:062709, 2014.

[8] T. Idema, J.O. Dubuis, L. Kang, M.L. Manning, P.C. Nelson, T.C. Lubensky, and A.J. Liu. The syncytial drosophila embryo as a mechanically excitable medium. *PLoS ONE*, 8(10):e77216, 2013.

[9] D. Sweeton, S. Parks, M. Costa, and E. Wieschaus. Gastrulation in *Drosophila*: the formation of the ventral furrow and posterior midgut invaginations. *Development*, 112:775–789, 1991.

[10] D.W. Howell, R.P. Behringer, and C.T. Veje. Fluctuations in granular media. *Chaos*, 9(3):559–572, 1999.

[11] R.P. Behringer, D. Howell, L. Kondic, S. Tennakoon, and C. Veje. Predictability and granular materials. *Physica D*, 133(1-4):1–17, 1999.

[12] S. Xie and A.C. Martin. Intracellular signalling and intercellular coupling coordinate heterogeneous contractile events to facilitate tissue folding. *Nat. Commun.*, 6:7161, 2015.

[13] M. Leptin. Gastrulation in drosophila: the logic and the cellular mechanisms. *EMBO J.*, 18(10):3187–3192, 1999.

[14] D. St Johnston and C. Nüsslein-Volhard. The origin of pattern and polarity in the drosophila embryo. *Cell*, 68:201–219, 1992.

[15] V. Riechmann and A. Ephrussi. Axis formation during drosophila oogenesis. *Curr. Opin. Genet. Dev.*, 11:374–383, 2001.

[16] J.-R. Huynh and D. St Johnston. The origin of asymmetry: Early polarisation of drosophila germline cyst and oocyte. *Curr. Biol.*, 14:R438–R449, 2004.

[17] F. van Eeden and D. St Johnston. The polarisation of the anterior-posterior and dorsal-ventral axes during drosophila oogenesis. *Curr. Opin. Genet. Dev.*, 9:396–404, 1999.

[18] M. Leptin and B. Grunewald. Cell-Shape Changes During Gastrulation in Drosophila. *Development*, 110(1):73–84, 1990.

[19] M Leptin. twist and snail as positive and negative regulators during Drosophila mesoderm development. *Genes & Development*, 5(9):1568–1576, 1991.

[20] Y.T. Ip, K. Maggert, and M. Levine. Uncoupling gastrulation and mesoderm differentiation in the Drosophila embryo. *EMBO J.*, 13(24):5826–5834, 1994.

[21] T.C. Seher, M. Narasimha, E. Vogelsang, and M. Leptin. Analysis and reconstitution of the genetic cascade controlling early mesoderm morphogenesis in the Drosophila embryo. *Mechanisms of Development*, 124(3):167–179, 2007.

[22] A.C. Martin, M. Kaschube, and E.F. Wieschaus. Pulsed contractions of an actin-myosin network drive apical constriction. *Nature*, 457(7228):495–499, 2009.

[23] A. Tordesillas, S.T. Tobin, M. Cil, K. Alshibli, and R.P. Behringer. Network flow model of force transmission in unbonded and bonded granular media. *Phys. Rev. E: Stat. Nonlinear Soft Matter Phys.*, 91(6):062204, 2015.

[24] L. Kondic, A. Goullet, C.S. O'Hern, M. Kramar, K. Mischaikow, and R.P. Behringer. Topology of force networks in compressed granular media. *EPL*, 97(5):54001, 2012.

[25] S. Tewari, D. Schiemann, D.J. Durian, C.M. Knobler, S.A. Langer, and A.J. Liu. Statistics of shear-induced rearrangements in a two-dimensional model foam. *Phys. Rev. E*, 60(4):4385–4396, 1999.

[26] D.J. Durian. Foam mechanics at the bubble scale. *Phys. Rev. Lett.*, 75(26):4780–4783, 1995.

[27] D.J. Durian. Bubble-scale model of foam mechanics: Melting, nonlinear behavior, and avalanches. *Phys. Rev. E: Stat. Nonlinear Soft Matter Phys.*, 55(2):1739–1751, 1997.

[28] S.A. Langer and A.J. Liu. Effect of random packing on stress relaxation in foam. *J. Phys. Chem. B*, 101(43):8667–8671, 1997.

[29] O. Polyakov, B. He, M. Swan, J.W. Shaevitz, M. Kaschube, and E. Wieschaus. Passive mechanical forces control cell-shape change during drosophila ventral furrow formation. *Biophys. J.*, 107:998–1010, 2014.

[30] J.R. Hove, R.W. Köster, A.S. Forouhar, G. Acevedo-Bolton, S.E. Fraser, and M. Gharib. Intracardiac fluid forces are an essential epigenetic factor for embryonic cardiogenesis. *Nature*, 421:172–177, 2003.

[31] J. Vermot, A.S. Forouhar, M. Liebling, D. Wu, D. Plummer, M. Gharib, and E. Fraser, S. Reversing Blood Flows Act through klf2a to Ensure Normal Valvulogenesis in the Developing Heart. *PLoS Biol.*, 7(11):e1000246, 2009.

[32] J.D. Bryngelson and P.G. Wolynes. Spin-glasses and the statistical-mechanics of protein folding. *Proc. Natl. Acad. Sci. U.S.A.*, 84(21):7524–7528, 1987.

[33] Z.Q. Li and H.A. Scheraga. Monte-Carlo-minimization approach to the multiple-minima problem in protein folding. *Proc. Natl. Acad. Sci. U.S.A.*, 84(19):6611–6615, 1987.

[34] K.F. Lau and K.A. Dill. A Lattice Statistical-Mechanics Model of the Conformational and Sequence-Spaces of Proteins. *Macromolecules*, 22(10):3986–3997, 1989.

[35] G. Foffi, G.D. McCullagh, A. Lawlor, E. Zaccarelli, K.A. Dawson, F. Sciortino, P. Tartaglia, D. Pini, and G. Stell. Phase equilibria and glass transition in colloidal systems with short-ranged attractive interactions: Application to protein crystallization. *Phys. Rev. E: Stat. Nonlinear Soft Matter Phys.*, 65(3, 1):031407, 2002.

[36] C.L. Lee, G. Stell, and J. Wang. First-passage time distribution and non-Markovian diffusion dynamics of protein folding. *J. Chem. Phys.*, 118(2):959–968, 2003.

[37] V.B.P. Leite, J.N. Onuchic, G. Stell, and J. Wang. Probing the kinetics of single molecule protein folding. *Biophys. J.*, 87(6):3633–3641, 2004.

[38] L. Davis and J.W. Chin. Designer proteins: applications of genetic code expansion in cell biology. *Nat. Rev. Mol. Cell Biol.*, 13(3):168–182, 2012.

[39] D.J. Mandell, M.J. Lajoie, M.T. Mee, R. Takeuchi, G. Kuznetsov, J.E. Norville, C.J. Gregg, B.L. Stoddard, and G.M. Church. Biocontainment of genetically modified organisms by synthetic protein design. *Nature*, 518(7537):55+, 2015.

[40] E. Procko, R. Hedman, K. Hamilton, J. Seetharaman, S.J. Fleishman, M. Su, J. Aramini, G. Kornhaber, J.F. Hunt, L. Tong, G.T. Montelione, and D. Baker. Computational Design of a Protein-Based Enzyme Inhibitor. *J. Mol. Biol.*, 425(18):3563–3575, 2013.

[41] I. Jain, M.M. Inamdar, and R. Padinhateeri. Statistical Mechanics Provides Novel Insights into Microtubule Stability and Mechanism of Shrinkage. *PLoS Comput. Biol.*, 11(2):UNSP e1004099, 2015.

[42] C. Heussinger, M. Bathe, and E. Frey. Statistical mechanics of semiflexible bundles of wormlike polymer chains. *Phys. Rev. Lett.*, 99(4):048101, 2007.

[43] D. Mizuno, C. Tardin, C.F. Schmidt, and F.C. MacKintosh. Nonequilibrium mechanics of active cytoskeletal networks. *Science*, 315(5810):370–373, 2007.

[44] T. Baumgart, A.T. Hammond, P. Sengupta, S.T. Hess, D.A. Holowka, B.A. Baird, and W.W. Webb. Large-scale fluid/fluid phase separation of proteins and lipids in giant plasma membrane vesicles. *Proc. Natl. Acad. Sci. U.S.A.*, 104(9):3165–3170, 2007.

[45] T. Baumgart, S.T. Hess, and W.W. Webb. Imaging coexisting fluid domains in biomembrane models coupling curvature and line tension. *Nature*, 425(6960):821–824, 2003.

[46] D. Lingwood and K. Simons. Lipid Rafts As a Membrane-Organizing Principle. *Science*, 327(5961):46–50, 2010.

[47] X. Morin, R. Daneman, M. Zavortink, and W. Chia. A protein trap strategy to detect GFP-tagged proteins expressed from their endogenous loci in Drosophila. *Proc. Natl. Acad. Sci. U.S.A.*, 98(26):15050–15055, 2001.

[48] M. Cavey and T. Lecuit. *Imaging cellular and molecular dynamics in live embryos using fluorescent proteins*, volume 420 of *Methods in Molecular Biology*. Humana Press Inc., Totowa, NJ, 2008.

[49] A.K. Spencer, B.A. Siddiqui, and J.H. Thomas. Cell shape change and invagination of the cephalic furrow involves reorganization of f-actin. *Dev. Biol.*, 402:192–207, 2015.

[50] L. Figard and A.M. Sokac. Imaging Cell Shape Change in Living Drosophila Embryos. *J. Vis. Exp.*, 49, 2011.

[51] C.A. Schneider, W.S. Rasband, and K.W. Eliceiri. NIH Image to ImageJ: 25 years of image analysis. *Nat. Methods.*, 9(7):671–675, 2012.

[52] G.-J. Gao, J. Blawzdziewicz, and C.S. O'Hern. Frequency distribution of mechanically stable disk packings. *Phys. Rev. E:*, 74:061304, 2006.